Dislocation density in cellular rapid solidification using phase field modeling and crystal plasticity

Matti Lindroos, Tatu Pinomaa, Kais Ammar, Anssi Laukkanen, Nikolas Provatas, Samuel Forest

To cite this version:

Matti Lindroos, Tatu Pinomaa, Kais Ammar, Anssi Laukkanen, Nikolas Provatas, et al.. Dislocation density in cellular rapid solidification using phase field modeling and crystal plasticity. International Journal of Plasticity, 2022, 148, pp.103139. 10.1016/j.ijplas.2021.103139 . hal-03589985

HAL Id: hal-03589985
https://hal.science/hal-03589985v1

Submitted on 26 Feb 2022

International Journal of Plasticity 148 (2022) 103139

Contents lists available at ScienceDirect

International Journal of Plasticity

journal homepage: www.elsevier.com/locate/ijplas

Dislocation density in cellular rapid solidification using phase field modeling and crystal plasticity

Matti Lindroos [*,a], Tatu Pinomaa [a], Kais Ammar [b], Anssi Laukkanen [a], Nikolas Provatas [c], Samuel Forest [b]

[a] *Integrated Computational Materials Engineering, VTT, Espoo, Finland*
[b] *MINES ParisTech, PSL University, MAT – Centre des matériaux, CNRS UMR 7633, BP 87 91003 Evry, France*
[c] *Department of Physics and Centre for the Physics of Materials, McGill University, Montreal, Canada*

ARTICLE INFO

Keywords:
Rapid solidification
Phase field method
Crystal plasticity
Residual stress
Dislocation structures

ABSTRACT

A coupled phase field and crystal plasticity model is established to analyze formation of dislocation structures and residual stresses during rapid solidification of additively manufactured 316L stainless steel. The work focuses on investigating the role of microsegregation related to the intragrain cellular microstructure of 316L. Effect of solidification shrinkage is considered along with dislocation mediated plastic flow of the material during solidification. Different cellular microstructures are analyzed and the characteristics of the cell core, boundary and segregation pools are discussed with respect to heterogeneity of dislocation density distributions and residual stresses. Quantitative comparison with experimental data is given to evaluate the feasibility of the modeling approach.

1. Introduction

Rapid solidification is a feature in several advanced industrial manufacturing techniques, such as thermal spray coating deposition (Lavernia and Srivatsan, 2010), certain welding techniques (David et al., 2003), and metal additive manufacturing (DebRoy et al., 2018). Rapid solidification alters microstructures through selection of metastable phases, solute trapping kinetics (Aziz, 1996; Cahn et al., 1998; Pinomaa et al., 2020a; 2021a), and changes in solidification morphology and length scales. An overlooked key feature of these microstructures is the formation of various types of crystalline defects (Balluffi et al., 2005). These include trapping of excess point vacancies (Zhang et al., 2017), formation of high dislocation densities (Bertsch et al., 2020; Wang et al., 2020; 2018; Zhang et al., 2021a; 2021b), high microstructural (type II-III) residual stresses (Chen et al., 2019), and lattice orientation gradients (Jreidini et al., 2021; Polonsky et al., 2020). As these crystalline defects critically affect materials' mechanical properties and performance, improving our understanding of these defect formation mechanisms is important.

While cast 316L steel suffers from relatively low yield strength (Lo et al., 2009), additively manufactured (AM) 316L can produce high yield strengths while preserving relatively high elongation to failure. These exceptional properties of AM 316L steel are primarily attributed primarily to the subgrain cellular microstructure that develops during rapid solidification (Gorsse et al., 2017; Krakhmalev et al., 2018; Qiu et al., 2018; Shamsujjoha et al., 2018; Sun et al., 2018; Voisin et al., 2021; Wang et al., 2018). Recent work by (Bertsch et al., 2020) suggest that geometrical constraint around the solidification melt pool, coupled to thermal contraction, plays a central role

---

[*] Corresponding author.
E-mail address: matti.lindroos@vtt.fi (M. Lindroos).

https://doi.org/10.1016/j.ijplas.2021.103139
Received 16 August 2021; Received in revised form 11 October 2021;
Available online 4 November 2021

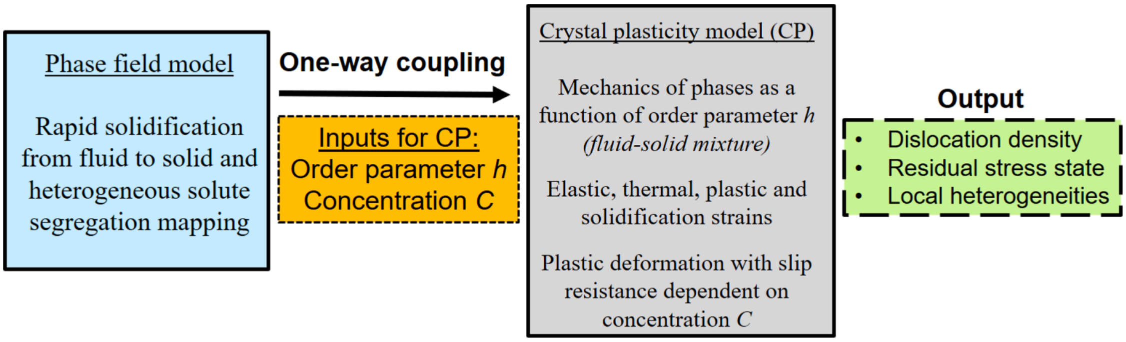

Fig. 1. Modeling approach with one-way coupled phase field and crystal plasticity models.

in formation of dislocations within the cellular solidification structures.

While there has been significant progress in understanding the micromechanics of additively manufactured stainless steels (Bronkhorst et al., 2019; Li et al., 2019; Pokharel et al., 2019; Voisin et al., 2021; Wang et al., 2018), there is lack of clarity regarding the formation of dislocations during rapid solidification and their evolution during loading, as well as the overall importance of different microstructure features (cell spacing, microsegregation, dislocations structures, grain boundaries) in forming the unique mechanical properties of AM 316L steel. Moreover, the link to material performance features such as fatigue life, remains somewhat unclear. Overall, there is still a knowledge gap between process conditions, rapid solidification microstructures and micromechanical response; this is reflected in a significant variation in the reported mechanical properties (yield strength, elongation to failure) for AM 316L steel materials reported in the literature (Casati et al., 2016; Qiu et al., 2018; Wang et al., 2018; Zhong et al., 2016).

Simulations of rapid solidification microstructure formation have been carried out extensively in the past (Chadwick and Voorhees, 2021; Pinomaa et al., 2020b; 2020c; Teferra and Rowenhorst, 2021; Yang et al., 2021; Zinovieva et al., 2020). To further understand the material behavior, crystal plasticity has been actively used to analyze mechanical response of AM 316L and other AM materials. For example, (Wang et al., 2018) performed tensile test simulations focusing on plastic behavior to identify yield and hardening parameters, while excluding deformation twinning and damage behavior taking place at higher strains. (Bronkhorst et al., 2019) focused on detailed analysis in defining crystal plasticity parameters from experimental datasets and to investigated the deformation response of realistic image based microstructures. To address the hierarchical microstructure, (van Nulund et al., 2021) employed a subgraining technique with crystal plasticity to capture intra-grain variations in 316L microstructure with no specific focus on the incorporation any special effects from microsegregation or voids. For the assessment of the as-printed state of solidified material, residual stress analysis has been performed with crystal plasticity to explain experimental measurements in AM 316L (Chen et al., 2019), as its prediction is crucial for AM parts.

Similarly, other additively manufactured materials require insight of segregations, formation of microscale defects, directionally solidified polycrystalline structure when modeling is considered (Lindroos et al., 2021). One option is to utilize phase field models to feed subsequent mechanical models. To couple mechanical and phase field models in producing feasible workflows for predicting mechanical behavior of AM material, for example (Pinomaa et al., 2019) and (Liu et al., 2020) utilized grain growth phase field model to inform the mechanical models to analyze the behavior of the formed microstructure.

Overall from the crystal plasticity point of view, one key aspect is how to assign realistic initial dislocation density for the models and how it is distributed in the hierarchical cellular microstructure of AM 316L. In many cases, the intuitive assumption is to assign constant initial dislocation density for the computational grain structure based on available measurements and/or fitting to material's initial yield. It is a known characteristics of AM 316L that the dislocation density has a heterogeneous distribution depending on the cell structure involving significant microsegregation (Voisin et al., 2021; Wang et al., 2018). It is somewhat unclear how to obtain and make use of these local intra-grain variations in dislocation densities for the AM 316L material.

In this paper, we present a phase field - crystal plasticity (PF-CP) coupled model for simulating rapid solidification of 316L steel with a focus on the intra-grain solidification phenomena, covering solidification cell growth and microsegregation, and how this leads to microscale solidification shrinkage, which triggers plastic deformation and formation of dislocation structures. A range of typical AM process conditions is considered by varying the thermal gradient G and solidification velocity V. Mechanical properties of the generated rapid solidification microstructures are investigated, where the role of dislocations and residual stresses are highlighted. The key novel feature of the study is that we estimate dislocation density distribution formed through microstructural solidification shrinkage under the heterogeneity resulting from solidification cells and the associated microsegregation.

First the overall computational framework is introduced, followed by descriptions of the rapid solidification phase field and the crystal plasticity models. In the results, solute segregation is analyzed as a function of the cooling rate (G and V) and three different solidification cases are investigated with a crystal plasticity model. A quantitative comparison of the predicted dislocation densities to experimental observations from literature is performed. The limitations and future aspects of the computational method are discussed in the final section. Appendix A provides additional results on the effect of model parameters and boundary conditions.

2. Methods

2.1. Computational approach

One-way (weak) coupling of phase field solution of rapid solidification with crystal plasticity analysis of mechanics is constructed. The model framework is implemented in Zset software (www.zset-software.com) making use of the previous general efforts of coupled phase field and mechanical analysis of (Ammar et al., 2009; de Rancourt et al., 2016). The phase field simulations inform the crystal plasticity model where solidification shrinkage occurs, which generates microstructural residual stresses in the solid, leading to plastic deformation and generation of dislocations. Heterogeneous solid solution strengthening effects are incorporated in the crystal plasticity model formulation based on the microsegregation obtained from the phase field model. Hence the used approach is sequential and both methods utilize the same time stepping. Exchange of data between the models is possible with concurrent analysis, however, there is no backflow of data from CP to PF in the present work. Fig. 1 illustrates to main ingredients of the modeling approach.

The simulations were carried out using a regular mesh on a computational domain of 448 x 224 elements. One element size is 50 nm and as such the domain size is 22.4 μm x 12 μm. The size of the domain becomes close to typical grain size of the AM 316L. However, the present simulations focuses on only one intra-grain region without any neighbouring grain interactions. The choice of boundary conditions is discussed in the following sections.

2.2. Phase field model for solidification

A pseudobinary alloy phase field model, introduced by (Pinomaa et al., 2020b), is used to simulate the rapid solidification of 316L steel. We assume that the 316L stainless steel has a nominal composition of Fe-17wt%Cr-11wt%Ni-2.5wt%Mo. Although the equilibrium high-temperature phase is BCC ferrite, in rapid solidification the ferritic phase disappears completely due to kinetic preference of the austenitic FCC phase (David et al., 1987; Katayama and Matsunawa, 1984). Therefore, the only relevant phase transformation to be considered in rapid solidification of 316L steel is liquid to FCC.

The phase field model describes the alloy as an ideal dilute Fe-Cr binary system. Only the diffusion of chromium is considered, and other alloying elements (nickel and molybdenum) act as passive background elements that solely affect the phase field model material parameters: Fe-Cr pseudobinary liquidus slope and partition coefficient, and solid-liquid interface energy. Further justification of this pseudobinary approximation is provided by (Pinomaa et al., 2020b).

We adopt the Frozen Temperature Approximation (FTA), where the temperature distribution is represented as a constant thermal gradient G moving at a fixed pulling speed V:

$$T = T_l - G \cdot (x - Vt), \tag{1}$$

where T_l is the material liquidus temperature, where the corresponding cooling rate is $Q = G \cdot V$.

The phase field model describes the evolution of an order parameter ϕ (using limits $-1 \le \phi \le 1$) and the Cr concentration field c. The evolution equations of these two fields become:

$$\begin{aligned} \tau \frac{\partial \phi}{\partial t} &= \nabla \cdot \left[W^2 \nabla \phi + W |\nabla \phi|^2 \left(\sum_k^{x,y,z} \frac{\partial W}{\partial(\partial \phi / \partial k)} \widehat{e}_k \right) \right] \\ &\quad + \phi - \phi^3 - \frac{\lambda}{1 - k_e} \left(e^u - 1 - \frac{T_l - T}{|m_l^e| c_l^o} \right) \left(1 - \phi^2\right)^2, \end{aligned} \tag{2}$$

$$\frac{\partial c}{\partial t} = \nabla \cdot \left[D_L \, c \, q(\phi) \nabla u + a_t^{'} W_0 (1 - k_e) e^u \frac{\partial \phi}{\partial t} \frac{\nabla \phi}{|\nabla \phi|} \right], \tag{3}$$

$$e^u = \frac{c}{c_{eq}}, \;\; c_{eq} = \frac{1 + k_e - (1 - k_e) h(\phi)}{2}, \tag{4}$$

$$h(\phi) = \phi, \;\; q(\phi) = \left(\frac{1 - \phi}{2} + \frac{1 + \phi}{2} \frac{D_S}{D_L} \right) \Big/ c_{eq}, \tag{5}$$

where $\tau = \tau(\mathbf{n})$ is the anisotropic interface attachment time scale, $W = W(\mathbf{n})$ is the anisotropic interface width and W_0 is its magnitude, λ is the coupling constant, T is the temperature field, T_l is the liquidus temperature, m_l^e is the equilibrium liquidus slope, $D_{L/S}$ is the liquid/solid diffusion coefficient, c_l^o is the nominal chromium composition, and $a_t^{'}$ is the modified antitrapping coefficient (Pinomaa and Provatas, 2019):

$$a_t^{'} = \frac{1}{2\sqrt{2}} \left(1 - A\left(1 - \phi^2\right)\right), \tag{6}$$

where A is *trapping parameter*, which is used to set a velocity-dependent partition coefficient and thereby to control the solute trapping behavior (Pinomaa and Provatas, 2019).

Table 1

Phase field model parameters for pseudobinary Fe-Cr approximation of 316L steel as an austenite-liquid system.

Equilibrium partition coefficient k_e	0.791 [a]
Equilibrium liquidus slope m_l^e	–3.49 K/wt% [a]
Alloy concentration c_l^o	17 wt%
Gibbs-Thomson coefficient Γ	3.47x10^{-7} K m
Latent heat L	1.25x10^{9} J/m^{3} [a]
Heat capacity C_p	5.46x10^{6} J/K/m^{3} [a]
Solutal capillary length d_0	43 nm
Liquid diffusion coefficient D_L	3.0x10^{-9} m^{2}/s [b]
Solid diffusion coefficient D_s	0 m^{2}/s
Kinetic coefficient β_0	0.269 s/m
Capillary anisotropy strength ϵ_c	0.018 (Bragard et al., 2002)
Kinetic anisotropy strength ϵ_k	0.13 (Bragard et al., 2002)
Solute trapping velocity V_D^{PF}	1.0 m/s (Smith and Aziz, 1994)
Computational interface width W_0	50 nm
Trapping parameter A	0.06
Element size dx	0.7W_0

[a] Thermo-Calc TCFE9 database (Andersson et al., 2002)

[b] Thermo-Calc MOBFE4 database (Andersson et al., 2002)

Matched asymptotic analysis by (Pinomaa and Provatas, 2019) relates parameters W, τ and λ in Eqs. (2,3) to solutal capillary length d_0 and kinetic coefficient β as follows:

$$d_0(\mathbf{n}) = a_1 \frac{W(\mathbf{n})}{\lambda} \tag{7}$$

$$\beta(\mathbf{n}) = a_1 \frac{\tau(\mathbf{n})}{\lambda\, W(\mathbf{n})} - a_1 a_2^- \frac{W(\mathbf{n})}{D_l}, \tag{8}$$

where $\mathbf{n} := \nabla\phi / |\nabla\phi|$ is the interface normal and a_1, a_2^- are asymptotic analysis constants that depend on the chosen interpolation functions $h(\phi)$ and $q(\phi)$. As presented by (Pinomaa and Provatas, 2019), for $h(\phi)$ and $q(\phi)$ given by Eq. 5 the asymptotic analysis constants are

$$a_1 = 0.8839 \tag{9}$$

$$a_2^- = \frac{8}{5\sqrt{2}}\left(\overline{K} + \overline{F}^-\right), \tag{10}$$

where a_2^- maps the phase field model onto the continuous growth sharp interface model corresponding to the case of full solute drag, and the constants in Eq. 10 are given by

$$\overline{K} \approx 0.0638 - 0.0505A, \tag{11}$$

$$\overline{F}^- = \frac{\sqrt{2}\ln 2}{2} + 3\frac{\sqrt{2}}{4}A. \tag{12}$$

Both the capillary length $d_0(\mathbf{n})$ and kinetic coefficient $\beta(\mathbf{n})$ are assumed to have weak anisotropy of cubic crystal lattices:

$$d_0(\mathbf{n}) / d_o^{mag} = 1 - 3\epsilon_c + 4\epsilon_c\left(n_x^4 + n_y^4 + n_z^4\right), \tag{13}$$

$$\beta(\mathbf{n}) / \beta_0 = 1 + 3\epsilon_k - 4\epsilon_k\left(n_x^4 + n_y^4 + n_z^4\right), \tag{14}$$

where d_0^{mag} is the magnitude of the capillary length $d_0(\mathbf{n})$, and ϵ_c is its anisotropy strength. Analogously, β_0 is the magnitude of the kinetic coefficient $\beta(\mathbf{n})$, and ϵ_k is its anisotropy strength.

The modified antitrapping coefficient of Eq. 6 results in a velocity-dependent non-equilibrium partition coefficient $k^{PF}(V)$ that follows a transcendental equation (Pinomaa and Provatas, 2019):

$$k^{PF}(V) = k_e \exp\left(\sqrt{2}\left(1 - k^{PF}(V)\right) V \middle/ V_D^{PF}\right), \tag{15}$$

Table 2
Crystal plasticity model parameters.

Young's modulus (solid) E^s	$-2.1005T^2 + 9.8491T + 65.69$ $[GPa]$
Poisson's ratio (solid) ν^s	0.27
Shear modulus (solid) μ	$E/(2(1 + \nu^s))$
Young's modulus (fluid) E^f	0.1 $[GPa]$
Poisson's ratio (fluid) ν^f	0.49
Solute strengthening term τ_{SS}^{ref}	$2.4449(c \cdot 18.0) + 8.39$ $[MPa]$[a]
Length of Burgers vector b^s	0.248 $[nm]$
Forest obstacle parameter K_{forest}	30.0
Coplanar obstacle parameter K_{coplan}	90.0
Annihilation distance G_c	4.96 $[nm]$
Hall-Petch coefficient K_{HP}	10.2 $[MPa\sqrt{mm}]$ (polycrystal)
Effective grain size polycrystal d_{grain}	15.9 $[\mu m]$
Interaction matrix coefficients $a_1 - a_6$	0.124,0.124,0.07,0.625,0.137,0.122
Viscous parameter for slip K	Equal to τ_{SS}^{ref} (polycrystal) and 1.0 for PF-CP
Strain rate parameter N	4.0
Thermal expansion α	$-\ 2.3062e^{-12}T^2 + 8.1149e^{-9}T + 1.2741e^{-5})$
Solidification strain components ϵ_0^s	$-\ 0.0125$

[a] c is the Cr concentration value in units of its nominal content (17 wt% in 316L). The used dependency on c is defined in (Pinomaa et al., 2020b). Interaction matrix values taken from ref. (Monnet and Mai, 2019).

where

$$V_D^{PF} = \frac{D_L}{AW_0} \tag{16}$$

is a characteristic solute trapping velocity, W_0 is the magnitude of anisotropic interface width $W(\mathbf{n})$. Eq. 15 can be solved numerically, and V_D^{PF} can be tuned to represent a specific amount of solute trapping based on experimental $k(V)$ data. Once an appropriate value for V_D^{PF} is chosen, the trapping parameter A in Eq. 6 is determined through Eq. 16. As we are not aware of direct measurements of solute trapping for iron alloys similar to ours, we assume that the solute trapping correlates with the material's equilibrium partition coefficient as proposed by (Smith and Aziz, 1994). Based on this we choose a continuous growth model diffusion velocity $V_D^{CGM} \approx 0.81$ m/s, corresponding to trapping velocity $V_D^{PF} \approx 1.0$ m/s; these partition coefficients are plotted in the Supplementary material A. All the relevant phase field model parameters are presented in Table 1.

The phase field equations are solved implicitly using Newton's method. The finite element mesh is uniformly spaced with square elements of size $dx = 0.7W_0$. For both order parameter and concentration evolution, we apply zero flux boundary conditions on all boundaries.

2.3. *Crystal plasticity model*

In the following, the single crystal plasticity model is presented. We impose a small deformation framework. Total strain is additively decomposed into elastic, plastic, solidification and thermal strain parts, respectively:

$$\underline{\epsilon} = \underline{\epsilon}^E + \underline{\epsilon}^P + \underline{\epsilon}^S + \underline{\epsilon}^T \tag{17}$$

Dislocation slip is considered as the dominant deformation mechanism. Deformation twinning (e.g., annealing twins) is not accounted for in present work for simplicity and due to uncertainty related to dominant parameters such as stacking fault energy with respect to micro-segregated local composition, especially at high temperatures. Solidification strain is included to produce shrinkage of the solidifying metal along with thermal strains.

The solidification shrinkage is computed with

$$\underline{\epsilon}^S = \epsilon_0^s \widetilde{h} \underline{I}, \tag{18}$$

where ϵ_0^s is axial dilation strain related to the relative density difference between solid and liquid, $\widetilde{h} = 1/2(1 + h(\{\phi\}))$ (based on Eq. 5), indicates the solid fraction based on the order parameters drawn from the phase field model, where $\widetilde{h}(-1) = 0$ (fluid) and $\widetilde{h}(1) = 1$ (solid), while intermediate values contain a mixture of solid and fluid. The solidification strain was set to produce approximately 4% volumetric shrinkage for the 316L material by adjusting parameter ϵ_0^s.

Thermal dilation is accounted with a thermal strain tensor:

$$\underset{\sim}{\epsilon}^T = \widetilde{h}\alpha\Delta T\underset{\sim}{I}, \tag{19}$$

where α is the thermal expansion coefficient and ΔT is the total change in local temperature.

In the solid phase, the elastic strain is used to compute the stress tensor by means of the isotropic Hooke law:

$$\underset{\sim}{\sigma} = \lambda \text{trace}\left(\underset{\sim}{\epsilon}^E\right)\underset{\sim}{I} + 2\mu\underset{\sim}{\epsilon}^E$$

where λ, μ are the Lamé constants which are computed from the Young modulus and Poisson ratio given in Table 2 for the solid phase. It would be more realistic to consider cubic elasticity for single crystal austenitic steel but this additional feature is left for future work.

Implicit Newton algorithm is used to integrate the evolution equations for the internal variables. Finally the elastic strain increment is computed as the difference to total strain rate:

$$\dot{\underset{\sim}{\epsilon}}^E = \dot{\underset{\sim}{\epsilon}} - \dot{\underset{\sim}{\epsilon}}^P - \dot{\underset{\sim}{\epsilon}}^S - \dot{\underset{\sim}{\epsilon}}^T$$

Plasticity velocity gradient is given by the sum of twelve $\{111\}\langle 110 >$ slip systems in austenite (FCC). Plasticity can occur whenever small amount of solid is present, i.e,. the scaled order parameter $\widetilde{h}$ is non-zero.

$$\dot{\underset{\sim}{\epsilon}}^p = \widetilde{h}\sum_{s=1}^{N_s=12}\dot{\gamma}^s\underset{\sim}{N}^s \tag{20}$$

where $\dot{\gamma}^s$ is the slip rate and $\underset{\sim}{N}^s$ is the orientation tensor of a slip system s. The slip rate is given by:

$$\dot{\gamma}^s = \left\langle\frac{|\tau^s| - \tau_c}{K}\right\rangle^N sign(\tau^s) \tag{21}$$

where τ^s is the resolved shear stress and τ_c is the effective slip resistance of a slip system s. K is a viscous parameter that can be chosen equal to τ_{SS} (defined below), and parameter N defines strain rate sensitivity and implicitly emulates dislocation climb effects which are heavily temperature activated.

The effective slip resistance (critical shear stress) is defined as

$$\tau_c = \tau_{SS} + \tau_{HP} + \mu b^s\sqrt{\sum a_{sj}\rho^j} \tag{22}$$

where τ_{SS} is the solid solution strengthening contribution, τ_{HP} contains the Hall-Petch like effect, μ is the shear modulus, b^s is the length of Burgers vector, a_{sj} is the interaction matrix, and ρ^j is the dislocation density. Negligibly low ($500\ m^{-2}$), but non-zero, dislocation density is assumed for the initial embryos of solid phase for numerical stability. Once deformation and plasticity, due to solidification, takes place, dislocation density can increase rapidly.

The Hall-Petch effect is given as a function of temperature:

$$\tau_{HP} = \frac{\mu}{\mu_{ref}}\frac{K_{HP}}{\sqrt{d_{grain}}}, \tag{23}$$

where μ_{ref} is the shear modulus in room temperature, K_{HP} is Hall-Petch coefficient, and d_{grain} is the effective grain size. Here, the determination of effective grain size during rapid solidification process is rather difficult since cell spacing has been shown to significantly affect the hardness of the material (Krakhmalev et al., 2018; Pinomaa et al., 2020b). Furthermore, the simulations focus on a representative intra-grain section, and not multiple grains nor grain boundaries. Therefore, we set the Hall-Petch effect to zero in the present PF-CP simulations. By definition, the length-scale imitating Hall-Petch offset term is often related to grain size of the polycrystal, and thus we assume that its effect becomes more relevant when a representative polycrystalline microstructure has actually formed.

The phase field model produces estimations of the solute segregation during solidification. The contribution of solid solution strengthening is then relevant to the heterogeneity of slip resistance and has a dominant role in the slip activation in the solid when assuming extremely low initial dislocation density. In the previous work of the authors (Pinomaa et al., 2020b), a CALPHAD-like solid solution strengthening model (Walbrühl et al., 2017) was used to determine its contribution to slip resistance. In the present context, however, the material strength is evaluated at very high temperatures. The accuracy of the approximation of solid solution strength is undeniably uncertain near solidus temperatures. To have an estimate for the temperature dependence of τ_{SS}, we relate its magnitude with the effective shear modulus with a temperature dependency in order to lower the solid solution resistance at high temperatures. This form resembles the temperature dependency placed for grain size effect in general. As such we are left with an expression:

$$\tau_{SS} = \frac{\mu}{\mu_{ref}}\tau_{SS}^{ref} \tag{24}$$

where τ_{SS}^{ref} is the solid solution strength at room temperature as a function of the solute concentration field. The evolution of dislocation density of slip system s (ρ^s) as a function of mean free path reads:

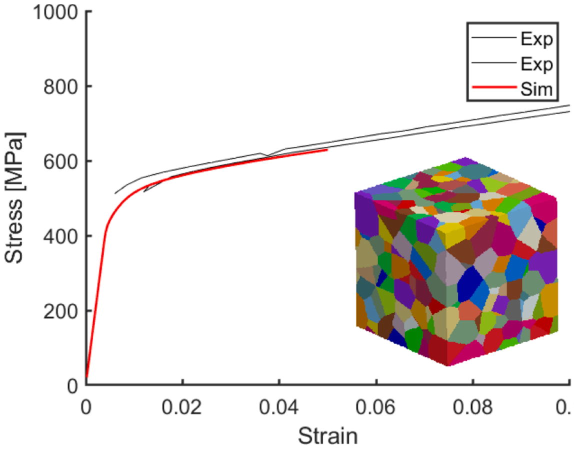

Fig. 2. Initial parameter identification for the crystal plasticity model at room temperature. Experimental curve taken from ((Bronkhorst et al., 2019; Gray III et al., 2017)).

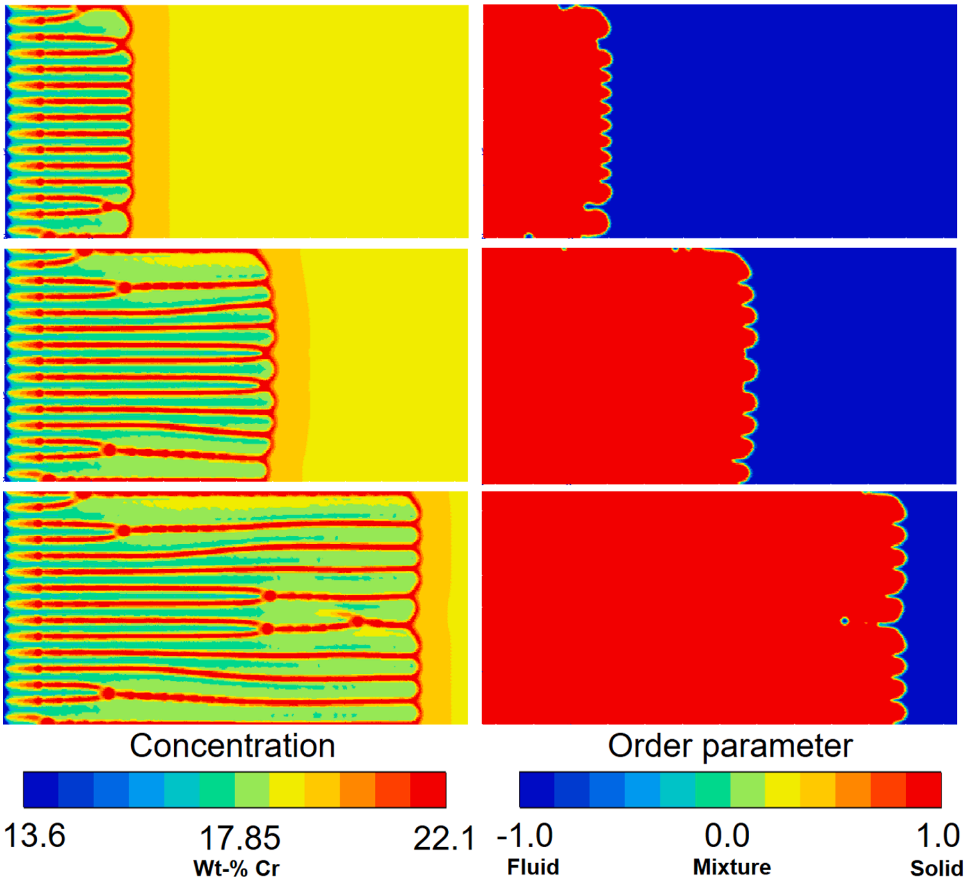

Fig. 3. Solute segregation and order parameter mappings during rapid solidification for $G = 10^6$ K/m and $V = 0.03$ m/s ($Q = 3 \times 10^3$ K/m).

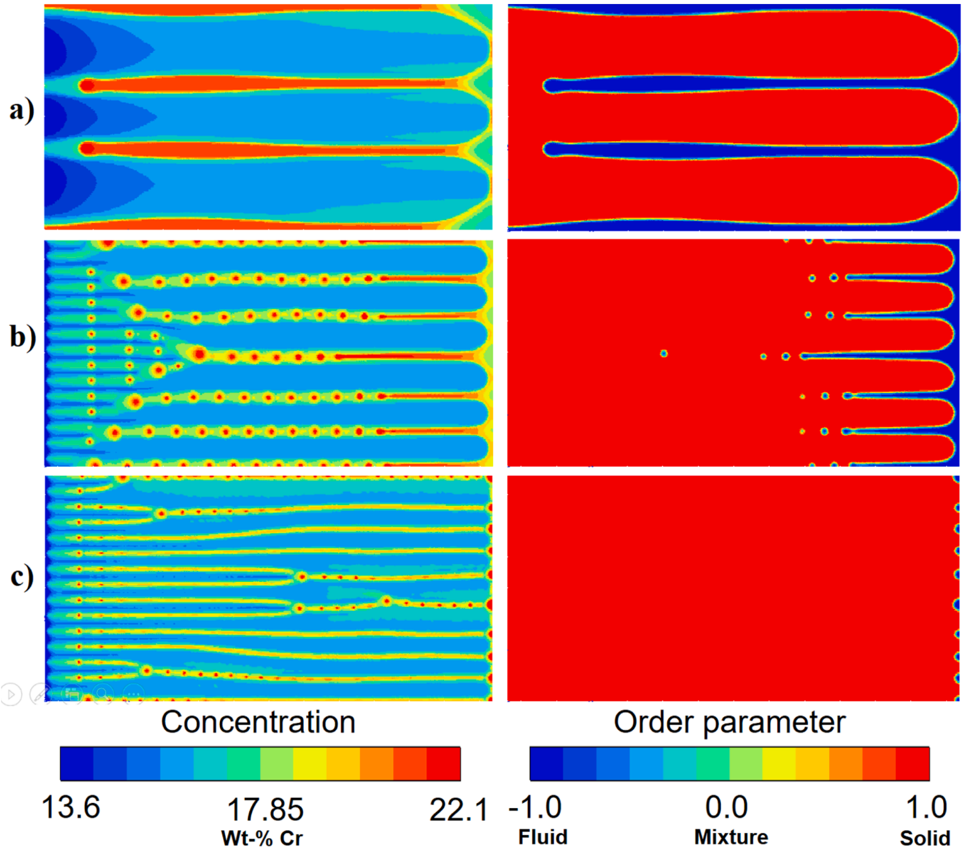

Fig. 4. Solute segregation and order parameter mappings at the end of simulation for a) $G = 10^5$ K/m and $V = 0.03$ m/s ($Q = 3 \times 10^3$ K/s), b) $G = 10^6$ K/m and $V = 0.012$ m/s ($Q = 12 \times 10^3$ K/s), c) $G = 10^6$ K/m and $V = 0.03$ m/s ($Q = 30 \times 10^3$ K/s).

$$\dot{\rho}^s = \frac{|\dot{\gamma}^s|}{b^s}\left[\frac{1}{d_{grain}} + \frac{\sqrt{\sum_{forest} a_{sj}\rho_j}}{K_{forest}} + \frac{\sqrt{\sum_{coplan} a_{sj}\rho_j}}{K_{coplan}} - G_c\rho^s\right], \tag{25}$$

where d_{grain} is the average grain size (set to ∞ here), and K_{forest} and K_{coplan} define the forest and co-planar dislocation hardening effects, respectively. They may be interpreted to describe the average number of obstacles passed by a dislocation before becoming immobile. Dislocation annihilation is controlled with a parameter G_c. It is notable that Eq. 25 describes the evolution of statistically stored dislocations (SSDs). The assumption of using only SSDs (and neglecting GNDs) is supported by recent analyses of AM 316L intragrain cellular dislocation substructures, where local intragrain misorientations were found to be negligible (Bertsch et al., 2020; Voisin et al., 2021).

The initial crystal plasticity model parameters were defined based on available stress-strain data at room temperature. Fig. 2 shows the initial parameter fitness with respect to experimental data (Bronkhorst et al., 2019; Gray III et al., 2017). A polycrystalline 3D microstructure was used with 500 randomly oriented grains in compression at a strain rate of 0.001 s^{-1}. The used microstructural cube is shown in Fig. 2. Voronoi tesselated grain structure with no specific grain elongation was assigned in the present case for simplicity. Kinematic uniform boundary conditions were applied, so that all faces of the volume element cube of the microstructure remain straight. The model response is in a reasonable agreement with the experimental curves in Fig. 2. The crystal plasticity model parameters are listed in Table 2. As pointed out, the Hall-Petch effect is set to zero in these small scale PF-CP simulations since the model operates generally below effective grain size scale and no neighbouring grains are taken into account in the solidification model or at the edges of the solid domain.

The solidification strain (shrinkage) is set to accomplish circa 4% volume change for the 316L material, as discussed above. Young's modulus, Poisson's ratio, thermal expansion, and shear modulus are set temperature dependent by fitting to data of (Kusnick et al., 2013). However, the minimum value of Young's modulus is restricted to 10 GPa. The fluid is treated as an isotropic elastic material with very low Young's modulus $E = 0.1$ GPa and quasi-incompressibility by taking $\nu = 0.49$. The concentration dependent τ_{SS}^{ref} is set constant in the polycrystal simulation during parameter fitting, using a concentration C value of 19.55 chromium $wt-\%$. This differs from the PF-CP simulations, where the concentration field (from phase field simulation) dictates the magnitude of τ_{SS}^{ref}, but the value 19.55 is a reasonable average value to be used for polycrystals. In general, we emphasize the relatively high uncertainty related to

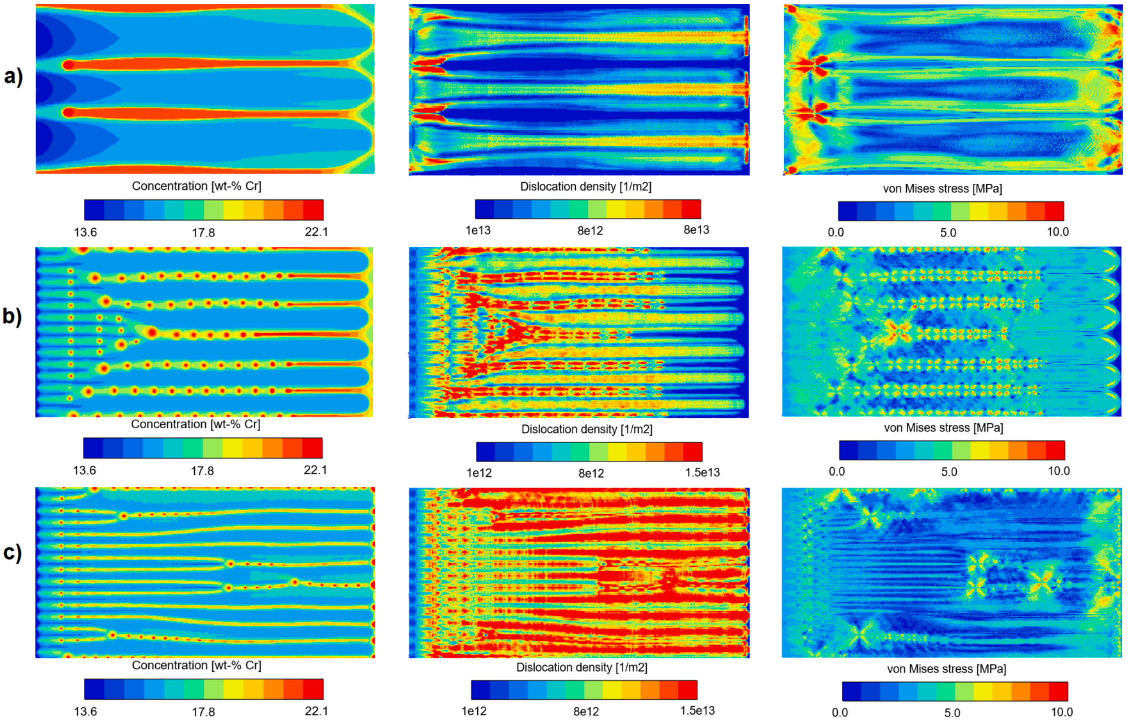

Fig. 5. Concentration of chromium, dislocation densities, and von Mises stress contours for a) $G = 10^5$ K/m and $V = 0.03$ m/s, b) $G = 10^6$ K/m and $V = 0.012$ m/s, c) $G = 10^6$ K/m and $V = 0.03$ m/s.

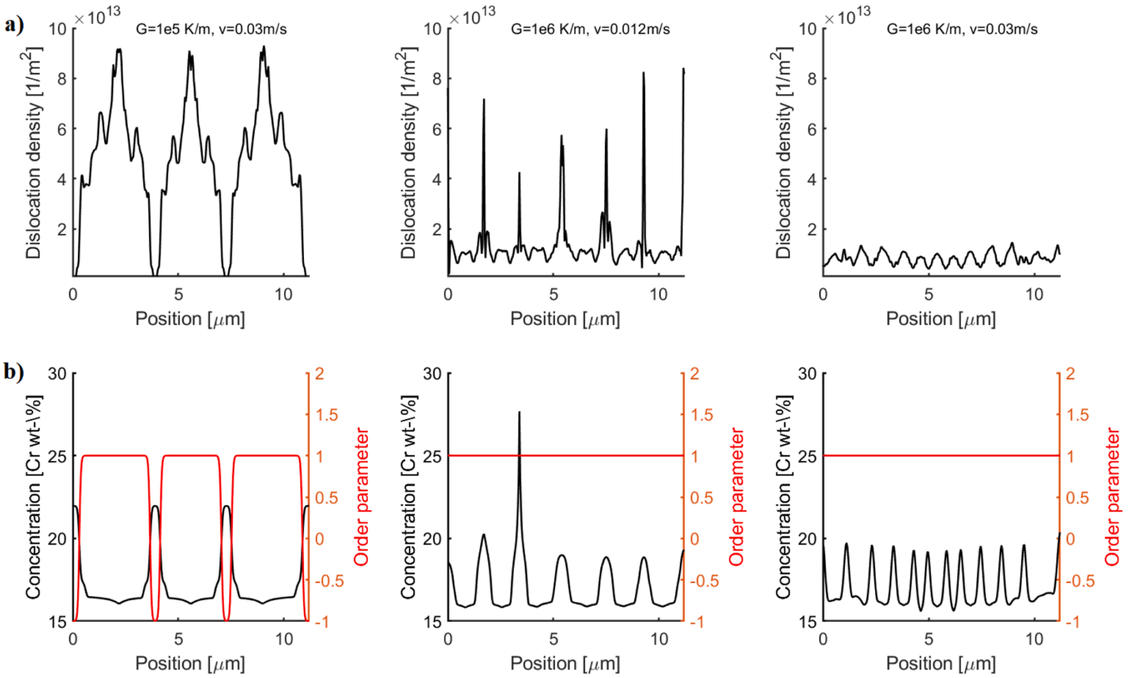

Fig. 6. Line profiles in the middle of the simulation box, in vertical direction, for the different cases, a) dislocation density with MPC boundary conditions, b) concentration (black) and order parameter (red) from PF simulations. (For interpretation of the references to colour in this figure legend, the reader is referred to the web version of this article.)

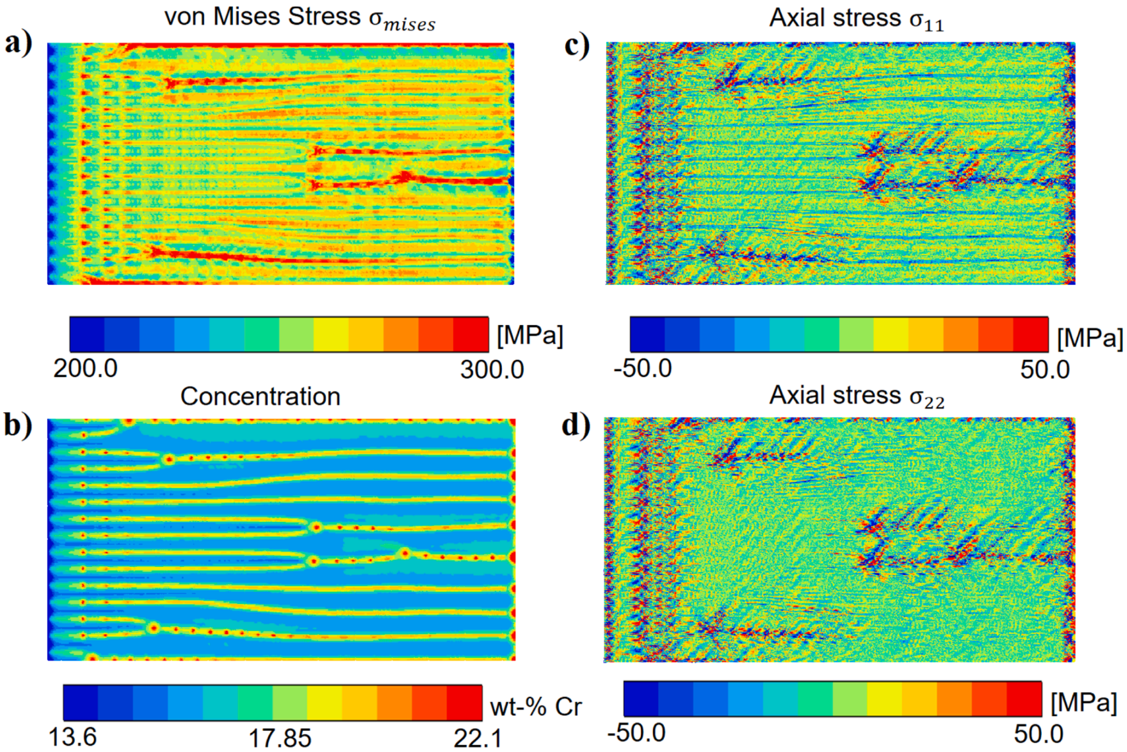

Fig. 7. Residual stress state after cooling to room temperature from near solidus temperature. a) von Mises stress, b) concentration, and axial stress components in c),d). (x and y directions, respectively).

model parameters at high temperatures during solidification that is its own separate topic of further study.

3. Results and discussion

3.1. Rapid solidification

The rapid solidification was performed by initializing a sinusoidal solid-liquid interface near the left boundary, and allowing for the frozen thermal gradient to drive the rapid solidification towards the right end of the boundary. This is shown in Fig. 3. The cells reach a quasi-steady size approximately midway through the simulation geometry. As cubic materials grow fastest in the [100] direction, we assume that the forming FCC solid is fully aligned with the thermal gradient, i.e. the solid [100] orientation is parallel to the simulation box x axis.

Three thermal gradient - pulling speed combinations were considered, representative of low-to-high cooling rates in metallic AM ((Pinomaa et al., 2020b)): 1) $G = 10^5$ K/m and $V = 0.03$ m/s ($Q = 3 \times 10^3$ K/s); 2) $G = 10^6$ K/m and $V = 0.012$ m/s ($Q = 12 \times 10^3$ K/s); and $G = 10^6$ K/m and $V = 0.03$ m/s ($Q = 30 \times 10^3$ K/s), as shown in Fig. 4. In all three cases, after an initial transient period, the solidification approaches a cellular growth form in quasi-steady state condition, meaning that the cell spacing approaches approximately a constant value. As expected, increasing the cooling rate ($Q = G \times V$) leads to a decrease in the cell spacing, the intercellular segregation, as well as the liquid fraction. A more detailed analysis of these simulated cellular structures, including more $G - V$ combinations, is found in (Pinomaa et al., 2020b). The chromium concentrations across the solidification cells (shown as line profiles in Fig. 6b) are consistent with recent measurements by (Bertsch et al., 2020), where chromium concentration was found to vary between roughly 17 wt% (cell core) and 20 wt% (cell boundary).

These rapid solidification simulations were coupled to a crystal plasticity model which predicts the formation of microstructural stresses, due to solidification shrinkage, and the associated generation of dislocations. As the model is one-way (weakly) coupled, the mechanical model does not feed any information back to the phase field solution. The micromechanical aspects are analyzed in what follows based on the phase field solution informing the state of solid-fluid mixture and the local solute concentration.

3.2. Crystal plasticity analysis

Fig. 5 shows segregation maps, the dislocation density and von Mises stress contours at the end of the simulations for different thermal gradients and pulling speeds. These phase field cases were selected to generate different solute segregation cell spacings, and represent typical low-to-high cooling rates in metallic AM. It should be noted that in Fig. 5a, the intercellular region is not fully solidified, whereas 5 b,c are mostly solidified in the critical regions for the analysis. As mentioned earlier, we assume that the crystal orientation is [100] in the horizontal direction of the simulation box and [010] in the vertical direction. The boundary conditions for CP are as follows: left side of the domain is fixed for lateral displacement, bottom edge is fixed for vertical displacement. Multi-point constraint is placed on the right side edge and top edges to retain rectangular shape of the domain. Alternative boundary conditions are evaluated in Appendix A. Periodic boundary conditions tends to generate artificially high dislocation densities at the domain edge regions. Free and MPC boundary conditions generate very similar magnitudes for total dislocation density without significant differences locally.

As the solid solution strengthening term (τ_{SS}) in slip resistance definition (Eq. 22) is constructed based on the local concentration, the dislocation evolution is greatly affected by the local variance in strength coming from microsegregation. The segregation cell cores with lower local concentration allow notable dislocation-mediated plasticity. Two main dislocation pile-up regions can be identified: 1) dislocation density is high near the cell boundaries but not exactly on center of the boundary, as seen in Fig. 5b), and 2) small and large segregation pools (often circular shaped) in Fig. 5b, with high concentration, have a tendency to form high dislocation densities. This develops residual stresses in the vicinity of the segregation pools in addition to the stress hot-spots observed near segregation cell boundaries with slightly lower magnitudes than the segregation pool regions. These segregation pools can potentially also form ferritic islands, which is not considered in this work. For the lowest cooling rate case, with residual liquid in the interdendritic regions remaining in Fig. 4a (see Fig. 4b for the order parameter), the cell cores channel dislocation density builds up, while the residual liquid zones having the highest solute concentrations relax their stresses and dislocation densities. The higher dislocation densities at intercellular regions, seen in Fig. 5, is consistent with SLM AM 316L structures seen by (Bertsch et al., 2020).

The line profiles in Fig. 6 visualize the accumulation heterogeneity of dislocations from cell core to intercellular boundaries with strong segregation. The dislocation densities vary between 0.5–8.4 $\times 10^{13}$ m^{-2} for the completely solidified cases (middle and right column in Fig. 6). Depending on the width of the segregation boundaries, dislocation density can exhibit a drop at the segregation cell boundaries (highest concentration). A noteworthy observation, already evident in the contours of Fig. 5, is that the cell boundary centers have a lower dislocation density, which is due to a higher slip resistance resulting from high solute concentration according to the imposed solid solution strengthening effects via the τ_{SS} term in Eq. 22. The line profiles show that the dislocation densities are generally 3–5 times higher than overall average due to existing microsegregation heterogeneities coming from the aforementioned large solidification cell boundaries and segregation pools. This is most visible with $G = 10^6$ K/m and $V = 0.012$ m/s (Fig. 5b, Fig. 6 middle column). An interesting feature is that the case $G = 10^6$ K/m and $V = 0.03$ m/s does not show as high local maxima as the other two cases. This could be explained by lower amount of concentration prone segregation pools, narrower cell cores and slightly lower cell boundary solute concentration. Overall, the heterogeneity related to dislocation distribution is significant in our simulations.

The aforementioned analysis focused on the rapid solidification and thermomechanics close to the solidus temperature. To further analyze the effect of cooling down the solidification microstructure, we advanced the thermomechanical PF-CP simulations to room temperature. Fig. 7 illustrates the residual stress state of the case $G = 10^6$ K/m and $V = 0.03$ m/s after it is further cooled down to room temperature. The same MPC boundary conditions are used, which allows relaxation of the top and right edge of the simulation box. The zones near left and right edge of the simulation domain should be excluded from the analysis due to partially incomplete solidification at the right edge and the sinusoidal initialization at the left edge. Only the mechanical (CP) model was cooled down to room temperature, while PF solution was arrested as shown in Fig. 4. The magnitude of axial stress components generally remain between -50 and 50 MPa. However, high stress concentrations are observed near segregation pools and at some of the cell boundaries exceeding of ± 100 MPa. Residual von Mises stress state show values above 200 MPa with some hotspots over 300 MPa. The observed residual stresses are plausible for the intra-grain configuration and are in the range of stresses reported by (Chen et al., 2019) with their experiments and complementing simulations. The simulation results regarding room temperature residual stress state of this work can be considered only as a preliminary estimation.

3.3. Quantitative comparison

Several authors have experimentally measured the dislocation densities using various complementary techniques. Even still, there are significant uncertainty sources associted with these techniques related to the sample preparation, instrumentation, as well as the assumptions made in estimating the dislocation densities. In selective laser melting of 316L steel, (Godec et al., 2020) measured a dislocation density of approximately 2.5 $\times$ 10^{14} m^{-2} with electron channeling contrast imaging (ECCI). Similarly, (Bronkhorst et al., 2019) measured an average value of 2.3 $\times$ 10^{14} m^{-2} for additively manufactured polycrystalline 316L at room temperature with synchrotron XRD. (Bertsch et al., 2020) measured a dislocation density of approximately 3–4 $\times$ 10^{14} in SLM 316L steel using line-intercept method. The simulations generally show a lower range of 0.5–9.0 $\times$ 10^{13} of the total dislocation density depending on local solute concentration. It is seen in Appendix A that dislocation densities exceeding $1.0 \times 10^{14}\ \mathrm{m}^{-2}$ are observed depending on the choice of model parameters, such as N, K, and τ_{SS}. It is also noteworthy that the dislocation density accumulation is sensitive to the formed cellular solidification structure, as expected. Possible reasons for the overall difference between experimentally observed values and simulations are discussed in the following section in more detail.

3.4. *Feasibility and future aspects*

There are several sources of uncertainties and aspects that need to be considered to improve the quantitative and predictive capability of the PF-CP framework presented in this paper. As a summary, these sources include the polycrystallinity, three-dimensionality, high temperature mechanical properties for the crystal plasticity model, as well as the mechanical boundary conditions.

Exact quantitative simulation results necessitate the consideration of a representative polycrystalline structure, where key phenomena are competitive grain growth, strong microsegregation as well as strain incompatibility at grain boundaries. These phenomena likely increase the microstructural stress (as well as dislocation density) heterogeneity and their overall magnitudes. In addition, extending the simulations to 3D is likely to be important for a realistic description of the highly irregular and morphologically complex grain structures present in metallic AM microstructures (Chadwick and Voorhees, 2021). Given the current 2D single crystal approach, future simulations in 3D, incorporating multiple grains to cover competitive growth of neighboring grains should be performed in for more precise quantitative comparison to experiments. The residual stress state is an interesting future topic to be considered with 3D simulations as well as when polycrystalline microstructure could be involved. At present, the chosen boundary conditions do not necessarily pose sufficient constraint of the formed surrounding microstructure as two edges of the domain are stiffly constraint and the remaining two, more or less, act as free surfaces.

In the crystal plasticity model used in this work, it was assumed that all dislocations were statistically stored dislocations. The crystal plasticity simulations did not incorporate lattice curvature effects, which can be an important feature in rapid solidification of 316L steel (Pinomaa et al., 2020b; Polonsky et al., 2020). Specifically, local misorientations between cells can form during plasticity, leading to generation of geometrically necessary dislocations, which would necessitate crystal plasticity models incorporating lattice curvature effects. However, recent characterization efforts of AM 316L steel cellular structures suggest that the local misorientation is negligible, implying that incorporating lattice curvature effects might not be crucial in modeling the formation of intragrain dislocation structures in AM 316L steels (Bertsch et al., 2020; Voisin et al., 2021), which is the scope of this paper.

However, the lattice curvature effects and orientation gradients (Polonsky et al., 2020) become important on the scale of polycrystals, in contrast to the dislocation formation associated with intragrain solidification cells. To describe multiple crystal orientations in phase field modeling framework, various approaches exist (Ofori-Opoku and Provatas, 2010; Pinomaa et al., 2021b; Steinbach and Pezzolla, 1999). Based on the PF-CP approach presented here, a multi-order parameter phase field model extension is exemplified elsewhere (Pinomaa et al., 2021a).

A notable source of uncertainty in these simulations is the high temperature mechanical properties of the 316L steel. To improve the predictive power of the crystal plasticity micromechanics in these solidification simulations, these mechanical properties, such as elastic properties and slip related parameters, should be extracted from appropriate experiments or, e.g., from molecular dynamics simulations. In addition, dislocation motion by climb was not separated in the total dislocation density evolution equations, and it is a significantly thermally activated mechanism (Balluffi et al., 2005). Instead, the effect of dislocation climb is implicitly considered through the exponent N in the power-law-type plasticity formulation. As an alternative, it could be incorporated in future quantitative simulations to possibly improve prediction capability of the model. These more detailed constitutive models that are widely established, however, they can quickly increase the number of crystal plasticity parameters which again arguably further increase uncertainty of choice/identification of each parameter. It was shown in Appendix A that accumulation of dislocation density is sensitive to certain model parameters, such as the solid solution strengthening term τ_{SS}, strain rate / dislocation climb parameter N. Other model parameters, e.g., viscous resistance with K, dislocation multiplication parameters K_{forest} - K_{coplan} and the annihilation distance G_c play also an important role in the evolution of dislocation density and could be assigned temperature dependent, as suggested for example in (Bronkhorst et al., 2019).

Another future topic is that it would be interesting to investigate the effect of thermal contraction the stability of the formed dislocation cells during cool-down and AM process thermal cycling, as well as how the dislocation motion is influenced by segregation elements such as Mo as well as pinning to precipitates and oxide inclusions (Voisin et al., 2021).

Overall, the presented phase field - crystal plasticity modeling framework leads to satisfactory agreement with available experiments in terms of the dislocation densities, and can be used to simulate the formation of solidification microstructures with manufacturing-generated microstructural residual stresses and dislocation density heterogeneity. As one application, this new simulation technique allows for more realistic structure-property-performance (Pinomaa et al., 2020b; 2019) type analyses for modeling based materials design.

4. Conclusions

A weak coupling between phase field simulation of rapid solidification involving solute segregation model was performed with crystal plasticity model to analyze the formation of dislocation structures in additively manufactured 316L steel. Different cooling rates produce variety of cellular segregation microstructures (i.e., cell-spacings) that are found very relevant in explaining the high strength of AM 316L. The main concluding remarks are summarized as:

- An effective demonstration was performed to analyze formation of dislocations in the solidified microstructure due to solidification shrinkage and local variations in material strength coming from intra-grain solute segregation. The coupled PF-CP modeling technique is found feasible to produce quantitative estimations of dislocation structures in cellular segregated microstructure. The technique is extendable to polycrystalline microstructures with or without significant solute strengthening mechanism.
- However, the total dislocation densities of the present simulations are found systematically lower than many experimental techniques report (ca. 1–9 × 10^{13} m^{-2} with respect to experimental values exceeding 1 × 10^{14} m^{-2}). Crystal plasticity model improvements could provide better estimations together when the model parameters can be effectively identified at high temperatures. Also, incorporation of grain-grain interaction is expected to be in an important role in 3D (computational) domains.
- Local solute segregation effectively generates a heterogeneous dislocation distribution in the microstructures. Dislocation density pile-up tend to form at intercellular region as well as near the cell boundaries. If segregation pools are formed, they act as effective pinning regions as dislocation density is found high around the pools. Residual stresses form a heterogeneous distribution depending on the microsegregation and associated with local dislocation densities.
- The modeling technique could be applied to produce valuable inputs for polycrystal level simulations requiring initial dislocation density mapping and/or local strength relationship with respect to manufacturing related intra-grain variations.

Author Statement

Author agreement for research paper “Dislocation density in cellular rapid solidification using phase field modeling and crystal plasticity”

We confirm that:

The paper is not concurrently submitted for publication elsewhere.

The paper, in its entirety, in part, or in a modifies version, has not been published elsewhere.

The paper has not previously been submitted for possible publication elsewhere.

Declaration of Competing Interest

The authors declare no conflict of interest on research work entitled “Dislocation density in cellular rapid solidification using phase field modeling and crystal plasticity’.’

Acknowledgment

ML, TP, and AL wish acknowledge the support of Academy of Finland through the HEADFORE project, Grant No. 333226. NP acknowledges the Natural Sciences and Engineering Research Council of Canada (NSERC) and the Canada Research Chairs (CRD) Program).

Appendix A. Sensitivity analysis

A1. Effect of model parameter N and K

Dislocation climb gains more relevance at high temperatures. The model parameter N indirectly describes these effects. The choice of value 15.0 in room temperature is reasonable. However, lower values such as 1.0–4.0 representing diffusion creep can better present high temperature behavior. Fig. A.8 shows the effect of parameter N. It is observed that value 4.0 tends to increase dislocation density slightly. However, a value 1.0 leads to lower accumulation of dislocation density near the cell boundaries and the dislocation density has a smoother distribution with respect to solute segregation seen in Fig. A.8a. All the following sensitivity analyses are performed for solidification with $G = 10^6$ K/m and $V = 0.012$ m/s ($Q = 12 \times 10^3$ K/s).

The effect of viscous parameter K is analyzed in Fig. A.9. Smaller value does not directly increase the total dislocation density by allowing easier flow. Most significant difference is observed when the value of K is set equal to τ_{SS}, which is also dependent on the evolution of local solute concentration C. When the solute concentration is low, higher dislocation density build up is observed. Local variance also in viscous resistance, through varying parameter K, influences the local maxima.

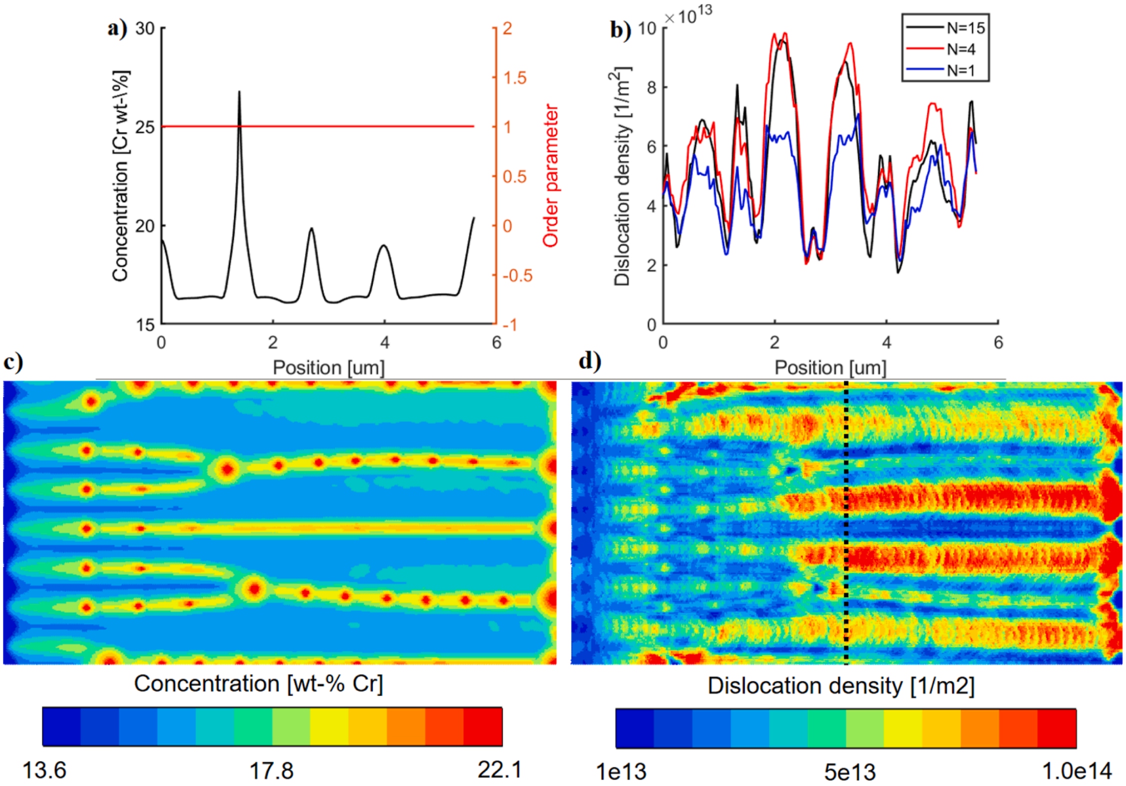

Fig. A.8. Sensitivity analysis on parameter N. a) Concentration and order parameter from PF, b) dislocation density over a line, c) concentration map, d) dislocation density map. Contours c) and d) are produced using $N = 1.0$.

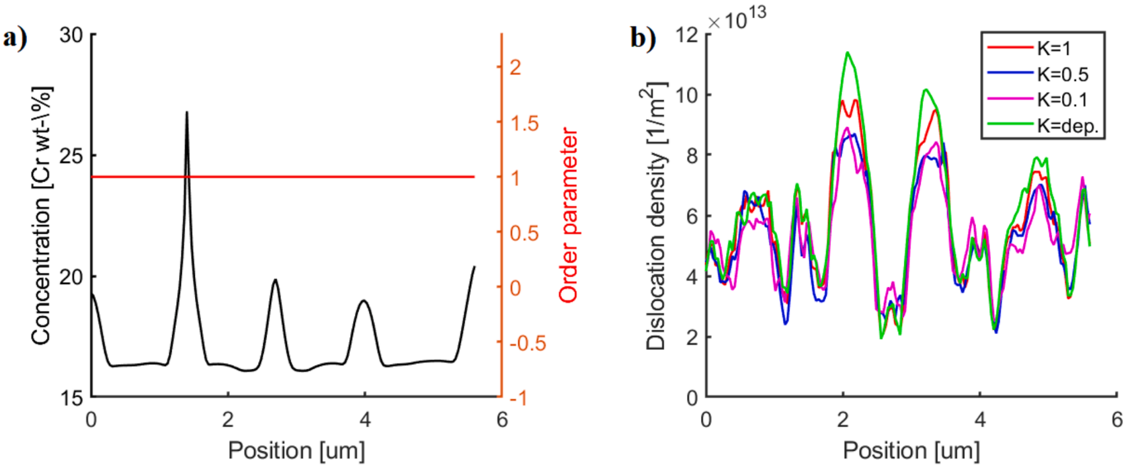

Fig. A.9. Sensitivity analysis on parameter K. a) Concentration and order parameter from PF and b) dislocation density over a line. Value for N is 4.0 except for the case where K is dependent on concentration C.

A2. *Effect of solid solution strengthening term*

There is an uncertainty in how solid solution strengthening effect evolves at high temperatures. We assumed a simple scaling rule by using $\tau_{SS} = \frac{\mu}{\mu_{ref}} \tau_{SS}^{ref}$ so that effective solid solution strength decrease with increasing temperature. This assumption does not necessarily hold. An analysis was performed to compare the τ_{SS} with the present assumption to four times smaller and larger τ_{SS} values, i.e., $\tau_{SS}^{modified} = 0.25\ \tau_{SS}$ or $\tau_{SS}^{modified} = 4.0\ \tau_{SS}$. Fig. A.10 shows line plot at the across of the simulation domain at position defined by a black dashed line in Fig. A.8(d). The accumulation of dislocation density is sensitive to the value of τ_{SS}. However, again low value does not

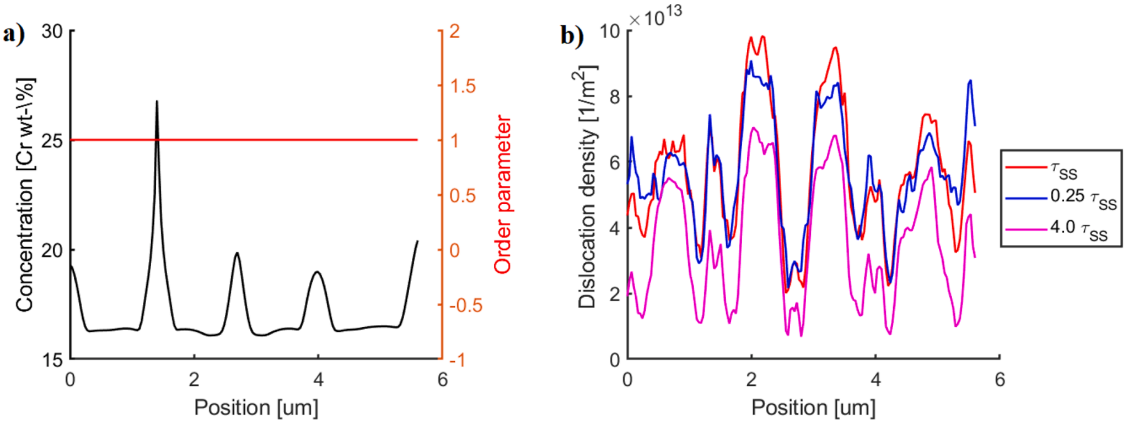

Fig. A.10. Sensitivity analysis on parameter τ_{SS}. a) Concentration and order parameter from PF, b) dislocation density over a line at the middle of the computational domain.

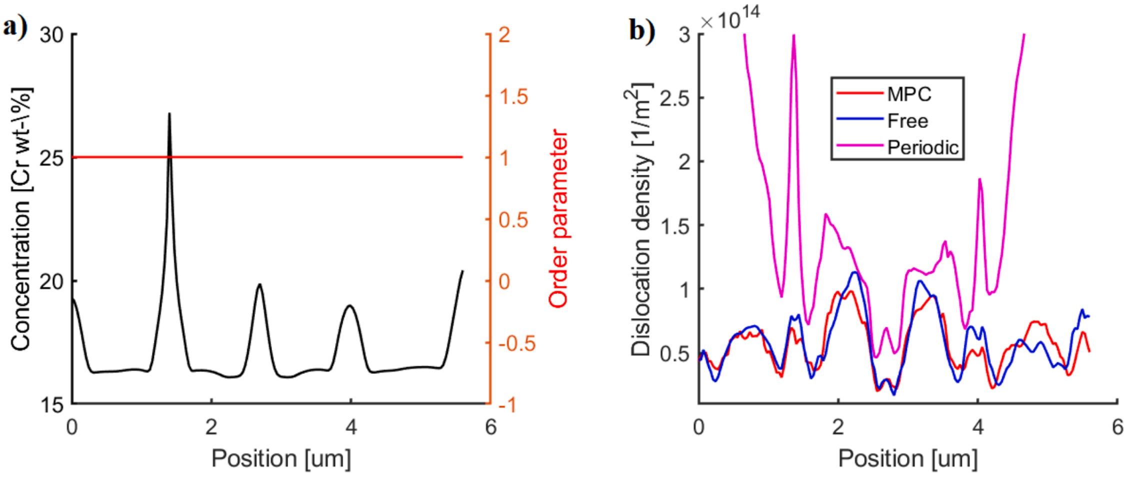

Fig. A.11. The effect of boundary conditions.

necessarily lead to higher dislocation density. Higher value, in turn, appear to decrease the maximum values near the cell boundaries. The strengthening effect through solute segregation then does not increase dislocation density at the cell core / boundary interface according to this sensitivity analysis.

A3. Effect of boundary conditions

Three different choices of boundary conditions are analyzed. With Free (BC) we impose lateral displacement (U1) zero at the left edge and horizontal displacement (U2) zero at the bottom edge of the computational domain. In addition to this, the second choice, Multi-point constraint (MPC) effectively restraints top and right edges of the domain to remain straight. In the present simulations the solidification occurs in 2D from left to right in the domain. This defines that the solidification takes places from left to right. With the third case, we define Periodic (BC) continuity is vertical top and bottom of the domain to define restrained continuity in-plane.

When compared to the MPC or free boundary condition, periodic boundary conditions lead to a larger geometrical constraint in the Y-direction (perpendicular to solidification direction), and thereby to larger dislocation densities. This trend is consistent with (Bertsch et al., 2020), where they conclude that thermal contraction and geometrical constraints play a key role in formation of large dislocation densities in AM 316L steels. There is only a small difference between free and MPC boundary conditions. However, we chose to use MPC in the computations of this paper in order to retain the edges of the computational domain straight. To this extent, it is expected that either free or MPC BCs are both likely presenting too soft behavior for the computational domain and further analysis of suitable BCs are required in future efforts.

References

Ammar, K., Appolaire, B., Cailletaud, G., Feyel, F., Forest, S., 2009. Finite element formulation of a phase field model based on the concept of generalized stresses. Comput. Mater. Sci 45, 800–805.

Andersson, J.-O., Helander, T., Höglund, L., Shi, P., Sundman, B., 2002. Thermo-calc & dictra, computational tools for materials science. Calphad 26 (2), 273–312.

Aziz, M.J., 1996. Interface attachment kinetics in alloy solidification. Metallurgical and materials transactions A 27 (3), 671–686.

Balluffi, R.W., Allen, S.M., Carter, W.C., 2005. Kinetics of Materials. John Wiley & Sons.

Bertsch, K., de Bellefon, G.M., Kuehl, B., Thoma, D., 2020. Origin of dislocation structures in an additively manufactured austenitic stainless steel 316l. Acta Mater 199, 19–33.

Bragard, J., Karma, A., Lee, Y.H., Plapp, M., 2002. Linking phase-field and atomistic simulations to model dendritic solidification in highly undercooled melts. Interface Sci. 10 (2–3), 121–136.

Bronkhorst, C., Mayeur, J., Livescu, V., Pokharel, R., Brown, D., Gray III, G., 2019. Structural representation of additively manufactured 316l austenitic stainless steel. Int. J. Plast. 118, 70–86.

Cahn, J.W., Carter, W.C., Johnson, W.C., 1998. The Selected Works of John W. Cahn. Wiley-TMS.

Casati, R., Lemke, J., Vedani, M., 2016. Microstructure and fracture behavior of 316l austenitic stainless steel produced by selective laser melting. Journal of Materials Science & Technology 32 (8), 738–744.

Chadwick, A.F., Voorhees, P.W., 2021. The development of grain structure during additive manufacturing. Acta Mater 211, 116862.

Chen, W., Voisin, T., Zhang, Y., Florien, J.-B., Spadaccini, C.M., McDowell, D.L., Zhu, T., Wang, Y.M., 2019. Microscale residual stresses in additively manufactured stainless steel. Nat Commun 10 (1), 1–12.

David, S., Babu, S., Vitek, J., 2003. Welding: solidification and microstructure. The Journal of The Minerals, Metals and Materials Society 55 (6), 14–20.

David, S., Vitek, J., Reed, R., Hebble, T., 1987. Effect of rapid solidification on stainless steel weld metal microstructures and its implications on the Schaeffler diagram. Technical Report. Oak Ridge National Lab., TN (USA).

DebRoy, T., Wei, H., Zuback, J., Mukherjee, T., Elmer, J., Milewski, J., Beese, A.M., Wilson-Heid, A., De, A., Zhang, W., 2018. Additive manufacturing of metallic components–process, structure and properties. Prog Mater Sci 92, 112–224.

Godec, M., Zaefferer, S., Podgornik, B., Šinko, M., Tchernychova, E., 2020. Quantitative multiscale correlative microstructure analysis of additive manufacturing of stainless steel 316l processed by selective laser melting. Mater Charact 160, 110074.

Gorsse, S., Hutchinson, C., Gouné, M., Banerjee, R., 2017. Additive manufacturing of metals: a brief review of the characteristic microstructures and properties of steels, ti-6al-4v and high-entropy alloys. Sci Technol Adv Mater 18 (1), 584–610.

Gray III, G., Livescu, V., Rigg, P., Trujillo, C., Cady, C., CM, C., Carpenter, J., Lienert, T., Fensin, S., 2017. Structure/property (constitutive and spallation response) of additively manufactured 316l stainless steel. Acta Mater 138, 140–149.

Jreidini, P., Pinomaa, T., Wiezorek, J., McKeown, J., Laukkanen, A., Provatas, N., 2021. Orientation gradients in rapidly solidified pure aluminum thin films: comparison of experiments and phase-field crystal simulations. Physical Review Letters (Accepted).

Katayama, S., Matsunawa, A., 1984. Solidification microstructure of laser welded stainless steels. International Congress on Applications of Lasers & Electro-Optics. LIA, pp. 60–67.

Krakhmalev, P., Fredriksson, G., Svensson, K., Yadroitsev, I., Yadroitsava, I., Thuvander, M., Peng, R., 2018. Microstructure, solidification texture, and thermal stability of 316 l stainless steel manufactured by laser powder bed fusion. Metals (Basel) 8 (8), 643.

Kusnick, J., Benson, M., Lyons, S., 2013. Finite element analysis of weld residual stresses in austenitic stainless steel dry cask storage system canisters. Techical Letter Report U.S. Nuclear Regulatory Commission, 1–31.

Lavernia, E.J., Srivatsan, T.S., 2010. The rapid solidification processing of materials: science, principles, technology, advances, and applications. J Mater Sci 45 (2), 287–325.

Li, Z., Voisin, T., McKeown, J.T., Ye, J., Braun, T., Kamath, C., King, W.E., Wang, Y.M., 2019. Tensile properties, strain rate sensitivity, and activation volume of additively manufactured 316l stainless steels. Int. J. Plast. 120, 395–410.

Lindroos, M., Pinomaa, T., Antikainen, A., Lagerbom, J., Reijonen, J., Lindroos, T., Andersson, T., Laukkanen, A., 2021. Micromechanical modeling approach to single track deformation, phase transformation and residual stress evolution during selective laser melting using crystal plasticity. Addit. Manuf. 38, 101819.

Liu, P., Wang, Z., Xiao, Y., Lebensohn, R., Liu, Y., Horstemeyer, M., Cui, X., Chen, L., 2020. Integration of phase-field model and crystal plasticity for the prediction of process-structure-property relation of additively manufactured metallic materials. Int. J. Plast. 128, 102670.

Lo, K.H., Shek, C.H., Lai, J., 2009. Recent developments in stainless steels. Materials Science and Engineering: R: Reports 65 (4–6), 39–104.

Monnet, G., Mai, C., 2019. Prediction of irradiation hardening in austenitic stainless steels: analytical and crystal plasticity studies. J. Nucl. Mater. 518, 316–325.

van Nulund, T., van Dommelen, J., Geers, M., 2021. Microstructural modeling of anisotropic plasticity in large scale additively manufactured 316l stainless steel. Mech. Mater. 153, 103664.

Ofori-Opoku, N., Provatas, N., 2010. A quantitative multi-phase field model of polycrystalline alloy solidification. Acta Mater 58 (6), 2155–2164.

Pinomaa, T., Laukkanen, A., Provatas, N., 2020. Solute trapping in rapid solidification. MRS Bull. 45 (11), 910–915.

Pinomaa, T., Lindroos, M., Jreidini, P., Haapalehto, M., Ammar, K., Wang, L., Forest, S., Provatas, N., Laukkanen, A., 2021. Multiscale analysis of crystalline defect formation in rapid solidification of pure aluminium and aluminium-copper alloys. Philosophical Transactions of the Royal Society A (Accepted).

Pinomaa, T., Lindroos, M., Walbrühl, M., Provatas, N., Laukkanen, A., 2020. The significance of spatial length scales and solute segregation in strengthening rapid solidification microstructures of 316l stainless steel. Acta Mater 184, 1–16.

Pinomaa, T., McKeown, J.M., Wiezorek, J.M., Provatas, N., Laukkanen, A., Suhonen, T., 2020. Phase field modeling of rapid resolidification of al-cu thin films. J Cryst Growth 532, 125418.

Pinomaa, T., Ofori-Opoku, N., Laukkanen, A., Provatas, N., 2021. Quantitative phase field simulations of polycrystalline solidification using a vector order parameter. Physical Review E 103 (5), 053310.

Pinomaa, T., Provatas, N., 2019. Quantitative phase field modeling of solute trapping and continuous growth kinetics in quasi-rapid solidification. Acta Mater 168, 167–177.

Pinomaa, T., Yashchuk, I., Lindroos, M., Andersson, T., Provatas, N., Laukkanen, A., 2019. Process-structure-properties-performance modeling for selective laser melting. Metals (Basel) 9 (11), 1138.

Pokharel, R., Patra, A., Brown, D.W., Clausen, B., Vogel, S.C., Gray III, G.T., 2019. An analysis of phase stresses in additively manufactured 304l stainless steel using neutron diffraction measurements and crystal plasticity finite element simulations. Int. J. Plast. 121, 201–217.

Polonsky, A.T., Lenthe, W.C., Echlin, M.P., Livescu, V., Gray III, G.T., Pollock, T.M., 2020. Solidification-driven orientation gradients in additively manufactured stainless steel. Acta Mater 183, 249–260.

Qiu, C., Al Kindi, M., Aladawi, A.S., Al Hatmi, I., 2018. A comprehensive study on microstructure and tensile behaviour of a selectively laser melted stainless steel. Sci Rep 8 (1), 7785.

de Rancourt, V., Appolaire, B., Forest, S., Ammar, K., 2016. Homogenization of viscoplastic constitutive laws within a phase field approach. J Mech Phys Solids 88, 291–319.

Shamsujjoha, M., Agnew, S.R., Fitz-Gerald, J.M., Moore, W.R., Newman, T.A., 2018. High strength and ductility of additively manufactured 316l stainless steel explained. Metallurgical and Materials Transactions A 49 (7), 3011–3027.

Smith, P.M., Aziz, M.J., 1994. Solute trapping in aluminum alloys. Acta Metall. Mater. 42 (10), 3515–3525.

Steinbach, I., Pezzolla, F., 1999. A generalized field method for multiphase transformations using interface fields. Physica D 134 (4), 385–393.

Sun, Z., Tan, X., Tor, S.B., Chua, C.K., 2018. Simultaneously enhanced strength and ductility for 3d-printed stainless steel 316l by selective laser melting. NPG Asia Mater. 1.

Teferra, K., Rowenhorst, D.J., 2021. Optimizing the cellular automata finite element model for additive manufacturing to simulate large microstructures. Acta Mater 116930.

Voisin, T., Forien, J.-B., Perron, A., Aubry, S., Bertin, N., Samanta, A., Baker, A., Wang, Y.M., 2021. New insights on cellular structures strengthening mechanisms and thermal stability of an austenitic stainless steel fabricated by laser powder-bed-fusion. Acta Mater 203, 116476.

Walbrühl, M., Linder, D., Ågren, J., Borgenstam, A., 2017. Modelling of solid solution strengthening in multicomponent alloys. Materials Science and Engineering: A 700, 301–311.

Wang, G., Ouyang, H., Fan, C., Guo, Q., Li, Z., Yan, W., Li, Z., 2020. The origin of high-density dislocations in additively manufactured metals. Materials Research Letters 8 (8), 283–290.

Wang, Y.M., Voisin, T., McKeown, J.T., Ye, J., Calta, N.P., Li, Z., Zeng, Z., Zhang, Y., Chen, W., Roehling, T.T., et al., 2018. Additively manufactured hierarchical stainless steels with high strength and ductility. Nat Mater 17 (1), 63.

Yang, M., Wang, L., Yan, W., 2021. Phase-field modeling of grain evolutions in additive manufacturing from nucleation, growth, to coarsening. npj Comput. Mater. 7 (1), 1–12.

Zhang, H., Liu, F., Yang, Y., Sun, D., 2017. The molecular dynamics study of vacancy formation during solidification of pure metals. Sci Rep 7 (1), 1–8.

Zhang, X., Knoop, D., Andrä, H., Harjo, S., Kawasaki, T., Lutz, A., Lahres, M., 2021. Multiscale constitutive modeling of additively manufactured Al–Si–Mg alloys based on measured phase stresses and dislocation density. Int. J. Plast. 140, 102972.

Zhang, X., Lutz, A., Andrä, H., Lahres, M., Gan, W., Maawad, E., Emmelmann, C., 2021. Evolution of microscopic strains, stresses, and dislocation density during in-situ tensile loading of additively manufactured AlSi10Mg alloy. Int. J. Plast. 139, 102946.

Zhong, Y., Liu, L., Wikman, S., Cui, D., Shen, Z., 2016. Intragranular cellular segregation network structure strengthening 316l stainless steel prepared by selective laser melting. J. Nucl. Mater. 470, 170–178.

Zinovieva, O., Zinoviev, A., Romanova, V., Balokhonov, R., 2020. Three-dimensional analysis of grain structure and texture of additively manufactured 316l austenitic stainless steel. Addit. Manuf. 36, 101521.